


# MicroMagnetic.jl: A Julia package for micromagnetic and atomistic simulations with GPU support

Weiwei Wang(王伟伟), Boyao Lyu(吕伯尧), Lingyao Kong(孔令尧), Hans Fangohr, and Haifeng Du(杜海峰)

**Citation:**Chin. Phys. B, 2024, 33 (**10**): 107508. DOI: 10.1088/1674-1056/ad766f
Journal homepage: http://cpb.iphy.ac.cn; http://iopscience.iop.org/cpb

**What follows is a list of articles you may be interested in**

---

## Skyrmion motion induced by spin-waves on magnetic nanotubes

Tijjani Abdulrazak, Xuejuan Liu(刘雪娟), Zhenyu Wang(王振宇), Yunshan Cao(曹云姗), and Peng Yan(严鹏)
Chin. Phys. B, 2024, 33 (**10**): 107504. DOI: 10.1088/1674-1056/ad5d64

## Mapping the antiparallel aligned domain rotation by microwave excitation

Jing Zhang(张景), Yuanzhi Cui(崔远志), Xiaoyu Wang(王晓雨), Chuang Wang(王创), Mengchen Liu(刘梦晨), Jie Xu(徐洁), Kai Li(李凯), Yunhe Zhao(赵芸鹤), Zhenyan Lu(陆振烟), Lining Pan(潘丽宁), Chendong Jin(金晨东), Qingfang Liu(刘青芳), Jianbo Wang(王建波), and Derang Cao(曹德让)
Chin. Phys. B, 2024, 33 (**9**): 097506. DOI: 10.1088/1674-1056/ad5536

## Creation and annihilation of artificial magnetic skyrmions with the electric field

Jun Cheng(程军), Liang Sun(孙亮), Yike Zhang(张一可), Tongzhou Ji(吉同舟), Rongxing Cao(曹荣幸), Bingfeng Miao(缪冰锋), Yonggang Zhao(赵永刚), and Haifeng Ding(丁海峰)
Chin. Phys. B, 2024, 33 (**3**): 037501. DOI: 10.1088/1674-1056/ad188f

## Magnonic band-pass and band-stop filters with structurally modulated waveguides

Lai-He Feng(冯来和), Mang-Yuan Ma(马莽原), Zhi-Hua Liu(刘智华), Kai-Le Xie(解凯乐), and Fu-Sheng Ma(马付胜)
Chin. Phys. B, 2023, 32 (**6**): 067503. DOI: 10.1088/1674-1056/ac8afb

## Gate-voltage control of alternating-current-driven skyrmion propagation in ferromagnetic nanotrack devices

Xin-Yi Cai(蔡心怡), Zhi-Hua Chen(陈志华), Hang-Xiao Yang(杨航霄), Xin-Yan He(何鑫岩), Zhen-Zhen Chen(陈珍珍), Ming-Min Zhu(朱明敏), Yang Qiu(邱阳), Guo-Liang Yu(郁国良), and Hao-Miao Zhou(周浩淼)
Chin. Phys. B, 2023, 32 (**6**): 067502. DOI: 10.1088/1674-1056/acb420

---

**COMPUTATIONAL PROGRAMS FOR PHYSICS**

# MicroMagnetic.jl: A Julia package for micromagnetic and atomistic simulations with GPU support

Weiwei Wang(王伟伟)[1,†], Boyao Lyu(吕伯尧)[2,3], Lingyao Kong(孔令尧)[4], Hans Fangohr[5], and Haifeng Du(杜海峰)[2,‡]

[1] *Institutes of Physical Science and Information Technology, Anhui University, Hefei* 230601, *China*
[2] *Anhui Province Key Laboratory of Low-Energy Quantum Materials and Devices, High Magnetic Field Laboratory, HFIPS, Chinese Academy of Sciences, Hefei* 230031, *China*
[3] *University of Science and Technology of China, Hefei* 230031, *China*
[4] *School of Physics and Optoelectronic Engineering, Anhui University, Hefei* 230601, *China*
[5] *University of Southampton, Southampton SO*17 1*BJ, United Kingdom*

(Received 23 June 2024; revised manuscript received 31 August 2024; accepted manuscript online 3 September 2024)

MicroMagnetic.jl is an open-source Julia package for micromagnetic and atomistic simulations. Using the features of the Julia programming language, MicroMagnetic.jl supports CPU and various GPU platforms, including NVIDIA, AMD, Intel, and Apple GPUs. Moreover, MicroMagnetic.jl supports Monte Carlo simulations for atomistic models and implements the nudged-elastic-band method for energy barrier computations. With built-in support for double and single precision modes and a design allowing easy extensibility to add new features, MicroMagnetic.jl provides a versatile toolset for researchers in micromagnetics and atomistic simulations.

**Keywords:** micromagnetic simulations, atomistic simulations, graphics processing units

**PACS:** 75.78.Cd, 75.40.Mg, 75.78.Fg, 75.40.Gb **DOI:** 10.1088/1674-1056/ad766f

## 1. Introduction

Micromagnetics[1,2] is an effective tool for studying magnetic structures and phenomena at the micrometer scale. With the fast development of high-performance computation, micromagnetic simulations have been applied in various technological applications, such as magnetic recording media, magnonics,[3,4] magnetic sensors, and spintronic devices.[5–7]

Micromagnetic simulation packages typically use two primary numerical methods: finite difference methods (FDM)[8] and finite element methods (FEM).[9] The FDM approach, as implemented in packages such as OOMMF,[10] MuMax3,[11] and fidimag,[12] offers simplicity in implementation and computational efficiency. The FEM, as employed in Magpar,[13] Nmag[14] and Commics,[15] provides more flexibility in handling complex geometries at the cost of increased computational complexity and setup efforts.

The rapid development of graphics processing units (GPUs), especially Nvidia's GPUs, has extensively promoted the development of high-performance computing. GPUs' parallelization capabilities have accelerated micromagnetic simulations. For example, MuMax3[11] uses Nvidia GPUs to speed up the micromagnetic calculations.

The micromagnetic packages fidimag[12] and magnum.np[16] are developed using the high-level language Python, which provide a uniform post-processing toolchain. Similarly, Julia's design prioritizes high performance and ease of use, making it well-suited for scientific tasks. Moreover, JuliaGPU[17] reuses Julia's existing CPU-oriented compiler to generate code for the GPU, allowing a subset of the language to be directly executable on the GPU. JuliaGPU initially supported only NVIDIA hardware accelerators via CUDA. However, with GPUCompiler.jl and LLVM, Julia's capabilities extend to various hardware platforms, including AMD, Intel, and Apple M-series GPUs.

MicroMagnetic.jl is an open-source Julia package developed under the MIT license and designed for micromagnetic and atomistic simulations. MicroMagnetic.jl can be installed directly using Julia's package manager `Pkg`. Using the KernelAbstractions.jl[18] library, MicroMagnetic.jl facilitates the creation of heterogeneous kernels for various backends within a unified framework.

MicroMagnetic.jl is built on a modular framework, allowing others in the micromagnetic community to easily integrate new physics modules. Currently, the micromagnetic module in MicroMagnetic.jl supports only the finite difference method. In the future, we plan to incorporate a finite element implementation. Additionally, we will expand the atomistic module to include more lattice structures and enable direct parameter input from first-principles calculations. Finally, we are preparing to introduce a visualization interface to allow users to view simulation results in real time.

[†]Corresponding author. E-mail: wangweiwei@ahu.edu.cn
[‡]Corresponding author. E-mail: duhf@hmfl.ac.cn

© 2024 Chinese Physical Society and IOP Publishing Ltd 

## 2. Design

Multiple dispatch in Julia enables dynamic method selection based on argument types, enhancing code flexibility and extensibility. In MicroMagnetic.jl, we define various types to make use of multiple dispatch. For example, the `FDMesh` stores the discretized grid information since we have used FDM to discretize the micromagnetic energies. Figure 1 shows the basic structure of MicroMagnetic.jl, which mainly contains three parts: standard micromagnetics, atomistic simulations, and additional tools like LETM, MFM and post-processing tools.

**Listing 1.** An example of the function-based interface: users can pass their own defined functions to MicroMagnetic.jl.

```
function circular_Ms(x, y, z)
    if x^2 + y^2 <= (50 nm)^2
        return 8.0e5
    end
    return 0.0
end

set_Ms(sim, circular_Ms)
```

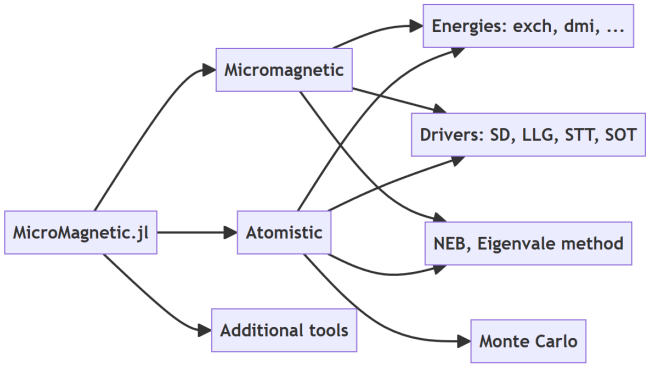



**Fig. 1.** The basic structure of MicroMagnetic.jl.

The micromagnetic parameters provided by the user include material properties, discretization details, and sample shapes. To provide users with maximum flexibility, almost all set functions in MicroMagnetic.jl can accept functions as parameters, as designed in Nmag,[14] FinMag[19] and fidimag.[12] For instance, the `set_Ms` function can be used to set the system's saturation magnetization. Moreover, it also can be used to define shapes. In Listing 1, we have defined a round disk, beyond which its saturation magnetization is 0. This cell-based approach enables users to define spatial parameters, offering maximum flexibility.

In addition to defining shapes using `set_Ms` function, MicroMagnetic.jl provides basic shapes and boolean operations to create regular shapes and their combinations, similar to MuMax3. Supported basic shapes in MicroMagnetic.jl include planes, cylinders, spheres, boxes, and torus. Figure 2 shows the boolean operations, including the union '+', the difference '−' and the intersection '∗' between a torus and a rotated box.

**Listing 2.** The Stoner–Wohlfarth model using the high-level interface sim_with.

```
using MicroMagnetic

args= (
    task = "relax",
    mesh = FDMesh(nx = 4, ny = 4, nz = 4),
    Ms = 1e6,
    A = 1e − 11,
    Ku = 5e4,
    axis = (1, 1, 0),
    stopping_dmdt = 0.05,
    H_s = [(i ∗ 5mT, 0, 0) for i in −20:20] )

sim_with(args)
```

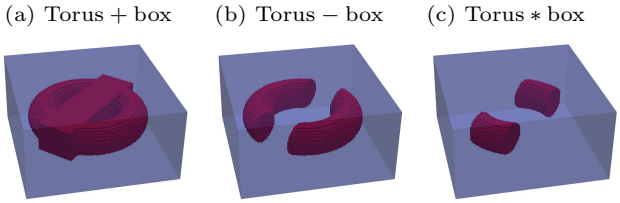



**Fig. 2.** The boolean operations of a torus and a rotated box: (a) the union '+', (b) the difference '−', and (c) the intersection '∗'.

Beyond the low-level API, which includes functions like `set_Ms`, we provide a high-level interface called `sim_with` to simplify the setup and execution of micromagnetic simulations. This interface allows users to encapsulate all relevant micromagnetic parameters into a `NamedTuple` or `Dict`, which can then be passed directly to `sim_with`. Listing 2 illustrates the use of `sim_with` for calculating the Stoner–Wohlfarth model. In this example, the external field $H$ is varied using the `_sweep` suffix (or `_s` for short). This `_s` syntax can similarly applied to other parameters, such as `Ms`, `Ku`, `A`, `D`, `task`, and `driver`, enabling the simulation to iterate over different values for these parameters. This approach provides the flexibility needed to explore a wide range of micromagnetic scenarios, including the computation of hysteresis loops and the investigation of parameter-dependent phenomena.

## 3. Micromagnetics

In the continuum theory, the magnetization $\boldsymbol{M}(\boldsymbol{r})$ is used to describe the average moment density over a local volume, and the total micromagnetic energy $E$ is a function of the magnetization $\boldsymbol{M}$. The effective field $\boldsymbol{H}_{\text{eff}}$ is defined as the functional derivative[1]

$$\boldsymbol{H}_{\text{eff}} = -\frac{1}{\mu_0 M_{\text{s}}} \frac{\delta E}{\delta \boldsymbol{m}}, \tag{1}$$

where $\boldsymbol{m} = \boldsymbol{M}(\boldsymbol{r})/M_{\text{s}}$ is the unit vector of the magnetization with $M_{\text{s}}$ the saturation magnetization.

### 3.1. Exchange energy

In the continuum limit, the isotropic exchange energy can be written as[8]

$$E_{\text{ex}} = \int_{\Omega} A(\nabla \boldsymbol{m})^2 \mathrm{d}x, \tag{2}$$

where $(\nabla \boldsymbol{m})^2 = (\nabla m_x)^2 + (\nabla m_y)^2 + (\nabla m_z)^2$. Therefore, the effective field for exchange interaction is

$$\boldsymbol{H}_{\text{ex}} = \frac{2A}{\mu_0 M_{\text{s}}} \nabla^2 \boldsymbol{m}. \tag{3}$$

Taking into account the standard 6-neighbors, the exchange energy density of cell $i$ reads[10]

$$w_i = \sum_{j \in N_i} A_{ij} \frac{\boldsymbol{m}_i \cdot (\boldsymbol{m}_i - \boldsymbol{m}_j)}{\Delta_{ij}^2}, \tag{4}$$

where $N_i$ denotes the set of 6 neighbors, $A_{ij}$ represents the exchange coefficient between cells $i$ and $j$, and $\Delta_{ij}$ is the discretization step size. $A_{ij} = A$ for the uniform exchange constant. MicroMagnetic.jl also supports the spatial exchange constant, i.e., cell-based exchange constant $A_i$ for cell $i$. Under this scenario $A_{ij} = 2A_iA_j/(A_i + A_j)$.[10] Consequently, the corresponding effective field can be computed as $\boldsymbol{H}_{\text{ex},i} = -1/(\mu_0 M_{\text{s}})(\partial w_i/\partial \boldsymbol{m}_i)$, yielding

$$\boldsymbol{H}_{\text{ex},i} = \frac{2}{\mu_0 M_{\text{s}}} \sum_{j \in N_i} A_{ij} \frac{\boldsymbol{m}_j - \boldsymbol{m}_i}{\Delta_{ij}^2}. \tag{5}$$

### 3.2. Magnetostatic energy

In micromagnetics, the magnetostatic energy, also referred to as demagnetization energy, is defined as

$$E_{\text{d}} = -\frac{\mu_0}{2} \int_V \boldsymbol{H}_{\text{d}}(\boldsymbol{r}) \cdot \boldsymbol{M}(\boldsymbol{r}) \mathrm{d}V, \tag{6}$$

where $\boldsymbol{H}_{\text{d}}$ denotes the demagnetizing field. Employing FDM, the demagnetization energy can be approximated as[8]

$$E_{\text{d}} \approx \frac{\mu_0}{2} \sum_{i,j} |V_i| \boldsymbol{M}(\boldsymbol{r}_i) \cdot \mathcal{N}(\boldsymbol{r}_i, \boldsymbol{r}_j) \cdot \boldsymbol{M}(\boldsymbol{r}_j), \tag{7}$$

where $|V_i| = \Delta_x \Delta_y \Delta_z$ represents the cell size, and the demagnetization tensor $\mathcal{N}(\boldsymbol{r}_i, \boldsymbol{r}_j)$ is a $3 \times 3$ matrix.[20] This tensor exhibits symmetry properties and is solely dependent on the distance between $\boldsymbol{r}_i$ and $\boldsymbol{r}_j$, denoted as $\mathcal{N}_{i-j} = \mathcal{N}(\boldsymbol{r}_i - \boldsymbol{r}_j) = \mathcal{N}(\boldsymbol{r}_i, \boldsymbol{r}_j)$. Consequently, one arrives at a discrete convolution for the demagnetizing field

$$\boldsymbol{H}_{\text{d},i} = -\sum_j \mathcal{N}_{i-j} \boldsymbol{M}_j, \tag{8}$$

which represents a cell-average field. The computation of the demagnetizing field can be sped up using FFT techniques.[21] The details of these techniques are clearly illustrated through discrete Fourier transforms.[22] Each demagnetization field calculation typically requires three forward Fourier transforms and three inverse Fourier transforms. However, by using the magnetic scalar potential, the three inverse Fourier transforms can be reduced to one.[23]

### 3.3. Dzyaloshinskii–Moriya energy

In the continuum limit, the Dzyaloshinskii–Moriya interaction (DMI) energy density $w_{\text{dmi}}$ is associated with the so-called Lifshitz invariants, which are terms in the form

$$L_{ij}^{(k)} = m_i \frac{\partial m_j}{\partial x_k} - m_j \frac{\partial m_i}{\partial x_k}. \tag{9}$$

The form of DMI energy density varies depending on the symmetry class. For bulk DMI found in materials such as MnSi[24] and FeGe,[25] corresponding to symmetry class $T$ or $O$, the expression is given by[16,26]

$$w_{\text{dmi}} = D(L_{yx}^{(z)} + L_{xz}^{(y)} + L_{zy}^{(x)}) = D\boldsymbol{m} \cdot (\nabla \times \boldsymbol{m}). \tag{10}$$

The associated effective field is

$$\boldsymbol{H}_{\text{dmi}} = -\frac{2D}{\mu_0 M_{\text{s}}} (\nabla \times \boldsymbol{m}). \tag{11}$$

For a thin film with interfacial DMI or a crystal with symmetry class $C_{nv}$, the energy density is[26]

$$w_{\text{dmi}} = D(L_{xz}^{(x)} + L_{yz}^{(y)}) = D\left(\boldsymbol{m} \cdot \boldsymbol{\nabla} m_z - m_z \boldsymbol{\nabla} \cdot \boldsymbol{m}\right), \tag{12}$$

and the effective field is

$$\boldsymbol{H}_{\text{dmi}} = -\frac{2D}{\mu_0 M_{\text{s}}} \left(\boldsymbol{e}_y \times \frac{\partial \boldsymbol{m}}{\partial x} - \boldsymbol{e}_x \times \frac{\partial \boldsymbol{m}}{\partial y}\right). \tag{13}$$

For a crystal with symmetry class $D_{2d}$, the DMI energy density is given by[26] $w_{\text{dmi}} = D(L_{xz}^{(y)} + L_{yz}^{(x)})$, resulting in the effective field

$$\boldsymbol{H}_{\text{dmi}} = -\frac{2D}{\mu_0 M_{\text{s}}} \left(\boldsymbol{e}_y \times \frac{\partial \boldsymbol{m}}{\partial y} - \boldsymbol{e}_x \times \frac{\partial \boldsymbol{m}}{\partial x}\right). \tag{14}$$

Although the effective fields for different symmetries differ, the numerical implementation can be unified as follows:

$$\boldsymbol{H}_{\text{dmi},i} = -\frac{1}{\mu_0 M_{\text{s}}} \sum_{j \in N_i} D_{ij} \frac{\boldsymbol{e}_{ij} \times \boldsymbol{m}_j}{\Delta_{ij}}, \tag{15}$$

where $D_{ij}$ represents the effective DMI constant and $\boldsymbol{e}_{ij}$ denotes the DMI vectors. For bulk DMI, $\boldsymbol{e}_{ij} = \hat{\boldsymbol{r}}_{ij}$, where $\hat{\boldsymbol{r}}_{ij}$ is the unit vector between cell $i$ and cell $j$. For interfacial DMI, $\boldsymbol{e}_{ij} = \boldsymbol{e}_z \times \hat{\boldsymbol{r}}_{ij}$, i.e., $\boldsymbol{e}_{ij} = \{-\boldsymbol{e}_y, \boldsymbol{e}_y, \boldsymbol{e}_x, -\boldsymbol{e}_x, 0, 0\}$ for the 6 neighbors $N_i = \{-x, +x, -y, +y, -z, +z\}$. For the symmetry class $D_{2d}$, one has $\boldsymbol{e}_{ij} = \{\boldsymbol{e}_x, -\boldsymbol{e}_x, -\boldsymbol{e}_y, \boldsymbol{e}_y, 0, 0\}$. If the cell-based DMI is provided, the effective DMI constant can be computed as $D_{ij} = 2D_iD_j/(D_i + D_j)$.[16]

### 3.4. Interlayer exchange interaction

In multilayer systems, indirect exchange interactions across ferromagnetic layers can occur in addition to the intralayer exchange interactions. The interlayer exchange interaction can be either symmetric (RKKY-type) or antisymmetric (DMI-type).[27,28] The energy density for the RKKY interaction is given by

$$w_{\text{rkky}} = -J_{\text{rkky}} \boldsymbol{m}_i \cdot \boldsymbol{m}_j, \tag{16}$$

where $J_{\text{rkky}}$ is the coupling constant between layer $i$ and layer $j$. The sign of $J_{\text{rkky}}$ depends on the thickness of the spacer layer. Similarly, the energy density for the interlayer DMI is

$$w_{\text{dmi-int}} = \boldsymbol{D}_{\text{int}} \cdot (\boldsymbol{m}_i \times \boldsymbol{m}_j), \tag{17}$$

where $\boldsymbol{D}_{\text{int}}$ is the DMI vector. The effective fields for the RKKY and interlayer DMI interactions are

$$\boldsymbol{H}_i = \frac{1}{\mu_0 M_{\text{s}}} \frac{J_{\text{rkky}}}{\Delta_z} \boldsymbol{m}_j, \quad \boldsymbol{H}_i = \frac{1}{\mu_0 M_{\text{s}}} \frac{\boldsymbol{D}_{\text{int}}}{\Delta_z} \times \boldsymbol{m}_j, \tag{18}$$

where $\Delta_z$ is the thickness of the cell.

## 4. Atomistic spin model

The fundamental assumption of the atomistic spin model is that each lattice site possesses a magnetic moment denoted by $\mu_{\text{s}}$. For metallic systems with quenched orbital moments, this magnetic moment primarily arises from its spin angular momentum, expressed as[29]

$$\boldsymbol{\mu} = -g\mu_{\text{B}} \boldsymbol{S} = -\hbar\gamma \boldsymbol{S}, \tag{19}$$

where $\mu_{\text{B}} = e\hbar/(2m)$ denotes the Bohr magneton, with $e\ (>0)$ the electron charge, $\gamma = g\mu_{\text{B}}/\hbar\ (>0)$ the gyromagnetic ratio, and $g = 2$ the $g$-factor. The magnetic moment can freely rotate in the three-dimensional space while maintaining a constant magnitude. Hence, the atomistic spin model is also referred to as the classical spin model.[30] Various interactions occur between magnetic moments, including exchange interaction $\mathcal{H}_{\text{ex}}$, anisotropy interaction $\mathcal{H}_{\text{an}}$, dipolar interaction $\mathcal{H}_{\text{d}}$, Dzyaloshinskii–Moriya interaction $\mathcal{H}_{\text{dmi}}$, and Zeeman interaction $\mathcal{H}_{\text{z}}$. The total Hamiltonian is the summation of these interactions[31]

$$\mathcal{H} = \mathcal{H}_{\text{ex}} + \mathcal{H}_{\text{dmi}} + \mathcal{H}_{\text{d}} + \mathcal{H}_{\text{an}} + \mathcal{H}_{\text{z}}. \tag{20}$$

The effective field $\boldsymbol{H}_{\text{eff}}$ can be computed from the total Hamiltonian $\mathcal{H}$

$$\boldsymbol{H}_{\text{eff}} = -\frac{1}{\mu_{\text{s}}} \frac{\partial \mathcal{H}}{\partial \boldsymbol{m}}, \tag{21}$$

where $\boldsymbol{m} = \boldsymbol{\mu}/\mu_{\text{s}}$ is the unit vector of magnetic moment $\boldsymbol{\mu}$. In general, parameters in the atomistic spin model can be established through two methods:[32] either via *ab initio* density functional theory calculations or determined experimentally.

### 4.1. Exchange interaction

The classical Heisenberg Hamiltonian with the nearest-neighbor exchange interaction is expressed as

$$\mathcal{H}_{\text{ex}} = -\sum_{\langle i,j \rangle} J_{ij} \boldsymbol{m}_i \cdot \boldsymbol{m}_j, \tag{22}$$

where $\langle i, j \rangle$ denotes a unique pair of lattice sites $i$ and $j$, and the summation is performed once for each pair. The exchange constant $J_{ij}$ characterizes the strength of the exchange interaction. A positive $J_{ij}$ favors the ferromagnetic state because the Hamiltonian [Eq. (22)] is minimized when the magnetic moments $\boldsymbol{m}_i$ and $\boldsymbol{m}_j$ are parallel, while a negative $J_{ij}$ leads to the antiferromagnetic state. The effective exchange field at site $i$ can be computed as

$$\boldsymbol{H}_{\text{ex},i} = \frac{1}{\mu_{\text{s}}} \sum_{\langle i,j \rangle} J_{ij} \boldsymbol{m}_j. \tag{23}$$

### 4.2. Dzyaloshinskii–Moriya interaction

In a more general form, the Hamiltonian of Heisenberg exchange [Eq. (22)] can be extended to[32]

$$\mathcal{H}_{\text{ex}} = -\sum_{\langle i,j \rangle} \boldsymbol{m}_i^{\text{T}} \hat{\mathcal{J}}_{ij} \boldsymbol{m}_j, \tag{24}$$

where $\hat{\mathcal{J}}_{ij} = \{J_{ij}^{\mu\nu}\}$ with $\mu, \nu = x, y, z$ is the exchange tensor. The diagonal part $\hat{\mathcal{J}}_{ij}^{\text{diag}}$ results in the isotropic exchange interaction [Eq. (22)]. Therefore, the exchange tensor $\hat{\mathcal{J}}_{ij}$ can be decomposed into three parts

$$\hat{\mathcal{J}}_{ij} = \hat{\mathcal{J}}_{ij}^{\text{diag}} + \hat{\mathcal{J}}_{ij}^{\text{s}} + \hat{\mathcal{J}}_{ij}^{\text{a}}, \tag{25}$$

where the traceless symmetric anisotropic exchange tensor $\hat{\mathcal{A}}_{ij}^{\text{s}}$ is defined by

$$\hat{\mathcal{J}}_{ij}^{\text{s}} = \frac{1}{2}(\hat{\mathcal{J}}_{ij} + \hat{\mathcal{J}}_{ij}^{\text{T}}) - \hat{\mathcal{J}}_{ij}^{\text{diag}}, \tag{26}$$

and the antisymmetric exchange matrix tensor is given by

$$\hat{\mathcal{J}}_{ij}^{\text{a}} = \frac{1}{2}(\hat{\mathcal{J}}_{ij} - \hat{\mathcal{J}}_{ij}^{\text{T}}). \tag{27}$$

Hence, the contribution to the Hamiltonian [Eq. (24)] from $\hat{\mathcal{J}}_{ij}^{\text{a}}$ can be recast into

$$\mathcal{H}_{\text{dmi}} = \sum_{\langle i,j \rangle} \boldsymbol{D}_{ij} \cdot (\boldsymbol{m}_i \times \boldsymbol{m}_j), \tag{28}$$

where $D_{ij}^x = J_{ij}^{zy} - J_{ij}^{yz}$, $D_{ij}^y = J_{ij}^{xz} - J_{ij}^{zx}$, and $D_{ij}^z = J_{ij}^{yx} - J_{ij}^{xy}$. This antisymmetric exchange interaction was first studied by Dzyaloshinskii (1958)[33] and Moriya (1960).[34] In general, the DMI can arise from the spin–orbit interaction and the vector $\boldsymbol{D}$ lies parallel or perpendicular to the line connecting the two spins. The parallel case $\boldsymbol{D}_{ij} = D\hat{\boldsymbol{r}}_{ij}$ corresponds to the bulk DMI and the perpendicular case $\boldsymbol{D}_{ij} = D\hat{\boldsymbol{r}}_{ij} \times \boldsymbol{e}_z$ corresponds to the interfacial DMI if both spins are located in the $xy$-plane.[35] The effective field of DMI can be computed as

$$\boldsymbol{H}_{\text{dmi},i} = -\frac{1}{\mu_{\text{s}}} \frac{\partial \mathcal{H}_{\text{dmi}}}{\partial \boldsymbol{m}_i} = \frac{1}{\mu_{\text{s}}} \sum_{\langle i,j \rangle} \boldsymbol{D}_{ij} \times \boldsymbol{m}_j. \tag{29}$$

### 4.3. Dipolar interaction

The dipolar interaction is a long-range interaction. The Hamiltonian for the dipolar interaction between magnetic moments $\boldsymbol{\mu}_i$ and $\boldsymbol{\mu}_j$ is

$$\mathcal{H}_{\mathrm{d}} = -\frac{\mu_0 \mu_{\mathrm{s}}^2}{4\pi} \sum_{i<j} \frac{3(\boldsymbol{m}_i \cdot \hat{\boldsymbol{r}}_{ij})(\boldsymbol{m}_j \cdot \hat{\boldsymbol{r}}_{ij}) - \boldsymbol{m}_i \cdot \boldsymbol{m}_j}{r_{ij}^3}, \quad (30)$$

where $r_{ij}$ is the distance between the two magnetic moments. Therefore, the corresponding effective field can be computed by

$$\boldsymbol{H}_{\mathrm{d},i} = \frac{\mu_0 \mu_{\mathrm{s}}}{4\pi} \sum_{i \neq j} \frac{3\hat{\boldsymbol{r}}_{ij}(\boldsymbol{m}_j \cdot \hat{\boldsymbol{r}}_{ij}) - \boldsymbol{m}_j}{r_{ij}^3}. \quad (31)$$

Similar to the micromagnetic case, the calculation of dipolar interaction can be sped up using FFT.

### 4.4. Anisotropy

In the presence of anisotropy, a magnetic moment tends to align along some preferred direction. Many physical effects can lead to an anisotropy, for instance, magnetocrystalline anisotropy can arise from the interaction between the local crystal environment and atomic electron orbitals.[32] The simplest form of the anisotropy is the so-called uniaxial anisotropy, and its Hamiltonian is given by

$$\mathcal{H}_{\mathrm{an}} = -K \sum_i (\boldsymbol{m}_i \cdot \boldsymbol{u})^2,$$

where the unit vector $\boldsymbol{u}$ is the easy axis and the constant $K$ represents the anisotropy strength. The corresponding effective field due to the uniaxial anisotropy is

$$\boldsymbol{H}_{\mathrm{an},i} = \frac{2K}{\mu_{\mathrm{s}}} (\boldsymbol{m}_i \cdot \boldsymbol{u}) \boldsymbol{u}. \quad (32)$$

Some materials, such as nickel, have a cubic crystal structure, which gives them a different form of anisotropy called cubic anisotropy. The Hamiltonian of cubic anisotropy is given by

$$\mathcal{H}_{\mathrm{an}}^{\mathrm{c}} = K_{\mathrm{c}} \sum_i (m_x^4 + m_y^4 + m_z^4). \quad (33)$$

By using the identity $m_x^2 + m_y^2 + m_z^2 = 1$, it is straightforward to see that the Hamiltonian [Eq. (33)] is equivalent to the form

$$\mathcal{H}_{\mathrm{an}}^{\mathrm{c}} = -2K_{\mathrm{c}} \sum_i (m_x^2 m_y^2 + m_y^2 m_z^2 + m_z^2 m_x^2). \quad (34)$$

### 4.5. Zeeman energy

The effective field of a magnetic moment in the presence of an external field $\boldsymbol{H}_{\mathrm{z}}$ is $\boldsymbol{H}_{\mathrm{z}}$ itself, which also can be seen from the Zeeman energy defined as

$$\mathcal{H}_{\mathrm{z}} = -\mu_{\mathrm{s}} \sum_i \boldsymbol{m}_i \cdot \boldsymbol{H}_{\mathrm{z}}. \quad (35)$$

## 5. LLG equation

The dynamics of magnetization or magnetic moments is governed by the Landau–Lifshitz–Gilbert (LLG) equation, which can be derived using the Lagrangian formulation with a Rayleigh's dissipation function:[36]

$$\frac{\partial \boldsymbol{m}}{\partial t} = -\gamma \boldsymbol{m} \times \boldsymbol{H}_{\mathrm{eff}} + \alpha \boldsymbol{m} \times \frac{\partial \boldsymbol{m}}{\partial t}. \quad (36)$$

The LLG equation (36) can be cast into the Landau–Lifshitz (LL) form

$$\frac{\partial \boldsymbol{m}}{\partial t} = -\frac{\gamma}{1+\alpha^2} \boldsymbol{m} \times \boldsymbol{H}_{\mathrm{eff}} - \frac{\alpha\gamma}{1+\alpha^2} \boldsymbol{m} \times (\boldsymbol{m} \times \boldsymbol{H}_{\mathrm{eff}}). \quad (37)$$

In practice, we need to use the LL form of the LLG equation [Eq. (37)] for numerical implementation. In MicroMagnetic.jl, to solve the LLG equation, we have implemented the adaptive Dormand–Prince method, a member of the Runge–Kutta family of ODE solvers.[37] Note that the typical Runge–Kutta method does not conserve the magnitude of magnetization. Therefore, a projection onto a unit sphere is taken after each successful step to enforce the constraint $|\boldsymbol{m}| = 1$.

### 5.1. Spin transfer torques

The discovery of giant magnetoresistance (GMR) shows that the resistance of a ferromagnetic conductor depends on its magnetization configuration. This suggests an interaction between the conduction electrons and the magnetization, which changes its electric conductivity. In the opposite direction, the flow of an electric current will affect the magnetization dynamics. Indeed, conduction electrons transfer the spin angular momentum to the magnetization of a ferromagnet.[38] Interestingly, Zhang and Li found that[39] most of the physics on the interplay between the magnetization dynamics of local moments and the spin-polarized transport of itinerant electrons can be captured mainly by the s–d model. The extended LLG equation with spin transfer torques (Zhang–Li model) is given by[39]

$$\begin{aligned} \frac{\partial \boldsymbol{m}}{\partial t} &= -\gamma \boldsymbol{m} \times \boldsymbol{H}_{\mathrm{eff}} + \alpha \boldsymbol{m} \times \frac{\partial \boldsymbol{m}}{\partial t} \\ &\quad - (\boldsymbol{u} \cdot \boldsymbol{\nabla}) \boldsymbol{m} + \beta [\boldsymbol{m} \times (\boldsymbol{u} \cdot \boldsymbol{\nabla}) \boldsymbol{m}]. \end{aligned} \quad (38)$$

Here, the parameter $\boldsymbol{u}$ is defined as

$$\boldsymbol{u} = -\frac{gP\mu_{\mathrm{B}}}{2eM_{\mathrm{s}}} \boldsymbol{j} = -\frac{Pg\mu_{\mathrm{B}} a^3}{2e\mu_{\mathrm{s}}} \boldsymbol{j}, \quad (39)$$

where $g$ is the Landé factor, $\mu_{\mathrm{B}}$ denotes the Bohr magneton, $e$ $(>0)$ represents the electron charge, $M_{\mathrm{s}}$ stands for the saturation magnetization, $P$ is the polarization rate of the current, and $\boldsymbol{j}$ denotes the current density. The $\beta$ term indicates the strength of nonadiabatic spin transfer torques, which is very important for the domain-wall motion.

In multilayers, the current flows perpendicular to the plane, which corresponds to the Slonczewski torque

$$\frac{\partial \boldsymbol{m}}{\partial t} = -\gamma \boldsymbol{m} \times \boldsymbol{H} + \alpha \boldsymbol{m} \times \frac{\partial \boldsymbol{m}}{\partial t}$$

$$-a_{\mathrm{J}}\boldsymbol{m}\times(\boldsymbol{m}\times\boldsymbol{p})-b_{\mathrm{J}}\boldsymbol{m}\times\boldsymbol{p}, \tag{40}$$

where $\boldsymbol{p}$ is a unit vector indicating the current polarization direction.

Although the physical origins of spin–orbit torque (SOT) are entirely different from spin transfer torque, the equation can still describe the mathematical form of SOT (40). Therefore, in MicroMagnetic.jl, we have implemented Eq. (40), where the user needs to provide parameters $a_{\mathrm{J}}$ and $b_{\mathrm{J}}$ to describe different physical processes.

Moreover, note that $-(\boldsymbol{u}\cdot\boldsymbol{\nabla})\boldsymbol{m}=\boldsymbol{m}\times[\boldsymbol{m}\times(\boldsymbol{u}\cdot\boldsymbol{\nabla})\boldsymbol{m}]$, so all the torques in the extended LLG equations (38) and (40) begin with $\boldsymbol{m}\times$. Therefore, these torques can be incorporated into the effective fields $\boldsymbol{H}_{\mathrm{eff}}$, which also simplifies the code structure.[40]

### 5.2. Thermal effects

When the spin system is connected to a thermal reservoir, the effect of temperature can be modeled by adding a stochastic field $\boldsymbol{\xi}$ to the effective field $\boldsymbol{H}_{\mathrm{eff}}$ in the standard LLG equation (36), forming the stochastic LLG (SLLG) equation. The thermal fluctuation is assumed to be a Gaussian white noise, i.e., the thermal noise $\boldsymbol{\xi}$ obeys the properties

$$\langle\boldsymbol{\xi}\rangle=0,\ \ \left\langle\boldsymbol{\xi}_i^u\cdot\boldsymbol{\xi}_j^v\right\rangle=2D\delta_{ij}\delta_{uv}, \tag{41}$$

where $i$ and $j$ are Cartesian indices, $u$ and $v$ indicate the magnetization components, and $\langle\cdot\rangle$ represents the average taken over different realizations of the fluctuating field. The constant $D=\alpha k_{\mathrm{B}}T/(\gamma\mu_{\mathrm{s}})$ denotes the strength of the thermal fluctuations. For the micromagnetic case, $D=\alpha k_{\mathrm{B}}T/(\mu_0 M_{\mathrm{s}}\gamma V_i)$ with $V_i$ the volume of the cell. The SLLG equation can be solved using numerical schemes.[22] Alternatively, an effective field can be incorporated into existing integrators:

$$\xi_i^u=\eta\sqrt{\frac{2\alpha k_{\mathrm{B}}T}{\mu_0 M_{\mathrm{s}}\gamma V_i\mathrm{d}t}}, \tag{42}$$

where $\eta$ is a random number following a normal distribution with a mean of 0 and a standard deviation of 1.

### 5.3. Cayley transform

The dynamics of magnetization evolves on a sphere $S^2$. Thus, there exists a $3\times3$ rotation matrix $\boldsymbol{Q}$ such that[41]

$$\boldsymbol{m}(t)=\boldsymbol{Q}(t)\boldsymbol{m}(0), \tag{43}$$

where $\boldsymbol{Q}(0)=\boldsymbol{I}$ is the identity matrix. Notice that the LLG equation (including the spin transfer torques) can be rewritten as

$$\frac{\partial\boldsymbol{m}}{\partial t}=\boldsymbol{f}(\boldsymbol{m})\times\boldsymbol{m}=\mathrm{skew}[\boldsymbol{f}]\boldsymbol{m}, \tag{44}$$

where $\boldsymbol{f}=\gamma(\boldsymbol{H}_{\mathrm{eff}}+\alpha\boldsymbol{m}\times\boldsymbol{H}_{\mathrm{eff}})/(1+\alpha^2)$ for the LLG equation and the contribution of spin transfer torques is $\boldsymbol{f}_{\mathrm{stt}}=[(\beta-\alpha)\boldsymbol{\tau}+(1+\alpha\beta)\boldsymbol{m}\times\boldsymbol{\tau})]/(1+\alpha^2)$ with $\boldsymbol{\tau}=(\boldsymbol{u}\cdot\nabla)\boldsymbol{m}$. The skew operator is defined as

$$\mathrm{skew}\,[\boldsymbol{x}]=\begin{pmatrix}0&-x_3&x_2\\x_3&0&-x_1\\-x_2&x_1&0\end{pmatrix}. \tag{45}$$

Therefore, the LLG equation becomes

$$\frac{\partial\boldsymbol{Q}}{\partial t}=\mathrm{skew}[\boldsymbol{f}]\boldsymbol{Q}(t). \tag{46}$$

Equation (46) can be further reformed using the Cayley transform, which is defined as

$$\boldsymbol{Q}=\left(\boldsymbol{I}-\frac{1}{2}\boldsymbol{\Omega}\right)^{-1}\left(\boldsymbol{I}+\frac{1}{2}\boldsymbol{\Omega}\right), \tag{47}$$

where $\boldsymbol{\Omega}=\mathrm{skew}[\boldsymbol{\omega}]$. The factor of $1/2$ in the Cayley transform can be changed to other nonzero numbers. Taking the derivative concerning time on both sides of Eq. (47) yields $(1/2)\dot{\boldsymbol{\Omega}}(\boldsymbol{Q}+\boldsymbol{I})=(\boldsymbol{I}-\frac{1}{2}\boldsymbol{\Omega})\dot{\boldsymbol{Q}}$. Noticed $\boldsymbol{Q}+\boldsymbol{I}=2(\boldsymbol{I}-\frac{1}{2}\boldsymbol{\Omega})^{-1}$, one obtains the decaying equation[42]

$$\frac{\partial\boldsymbol{\Omega}}{\partial t}=\boldsymbol{F}-\frac{1}{2}[\boldsymbol{\Omega},\boldsymbol{F}]-\frac{1}{4}\boldsymbol{\Omega}\boldsymbol{F}\boldsymbol{\Omega}, \tag{48}$$

where $\boldsymbol{F}=\mathrm{skew}\,[\boldsymbol{f}]$. In MicroMagnetic.jl, we make use of the vector form of Eq. (48), which reads

$$\frac{\partial\boldsymbol{\omega}}{\partial t}=\boldsymbol{f}-\frac{1}{2}(\boldsymbol{\omega}\times\boldsymbol{f})+\frac{1}{4}(\boldsymbol{\omega}\cdot\boldsymbol{f})\boldsymbol{\omega}. \tag{49}$$

Equation (49) can be integrated using the normal integration algorithms such as Runge–Kutta without worrying the conservation property.[41] It's worth mentioning that the absolute value of $\boldsymbol{\omega}$ will always increase for a nonzero $\boldsymbol{f}$. Therefore, restarting procedures are necessary to prevent $|\boldsymbol{\omega}|$ from becoming very large.[43]

## 6. Steepest descent energy minimization

A prevalent task in micromagnetics is finding the local energy minima states, for instance, calculating the hysteresis loops. The energy minimization process can be achieved by directly solving the LLG equation with a positive Gilbert damping. However, the steepest descent methods combined with step-size selected using Barzilian–Borwein rules have been proven a much more efficient way to find the local energy minima.[44,45] The MicroMagnetic.jl implementation of the steepest descent method uses the following update:

$$\boldsymbol{m}_{k+1}=\boldsymbol{m}_k-\tau_k\frac{\boldsymbol{m}_k+\boldsymbol{m}_{k+1}}{2}\times[\boldsymbol{m}_k\times\boldsymbol{H}_{\mathrm{eff}}(\boldsymbol{m}_k)], \tag{50}$$

which preserves the modulus of $\boldsymbol{m}$, i.e., $\boldsymbol{m}_{k+1}^2=\boldsymbol{m}_k^2$. Equation (50) explicitly gives

$$(1+\frac{\tau_k^2}{4}\boldsymbol{f}_k^2)\boldsymbol{m}_{k+1}=(1-\frac{\tau_k^2}{4}\boldsymbol{f}_k^2)\boldsymbol{m}_k-\tau_k\boldsymbol{g}_k, \tag{51}$$

where $\boldsymbol{f}_k = \boldsymbol{m}_k \times \boldsymbol{H}_{\text{eff}}$ and $\boldsymbol{g}_k = \boldsymbol{m}_k \times (\boldsymbol{m}_k \times \boldsymbol{H}_{\text{eff}})$. The step size $\tau_k$ can be chosen using Barzilian–Borwein rules

$$\tau_k^1 = \frac{\sum_i \boldsymbol{s}_{k-1}^i \cdot \boldsymbol{s}_{k-1}^i}{\sum_i \boldsymbol{s}_{k-1}^i \cdot \boldsymbol{y}_{k-1}^i}, \quad \tau_k^2 = \frac{\sum_i \boldsymbol{s}_{k-1}^i \cdot \boldsymbol{y}_{k-1}^i}{\sum_i \boldsymbol{y}_{k-1}^i \cdot \boldsymbol{y}_{k-1}^i}, \tag{52}$$

where $\boldsymbol{s}_{k-1} = \boldsymbol{m}_k - \boldsymbol{m}_{k-1}$ and $\boldsymbol{y}_{k-1} = \boldsymbol{g}_k - \boldsymbol{g}_{k-1}$.

## 7. Miscellaneous

In MicroMagnetic.jl, we provided a Markov chain Monte Carlo implementation for the atomistic spin model. The implemented Hamiltonian includes exchange interaction $\mathcal{H}_{\text{ex}}$, anisotropy interaction $\mathcal{H}_{\text{an}}$, Dzyaloshinskii–Moriya interaction $\mathcal{H}_{\text{dmi}}$, and Zeeman interaction $\mathcal{H}_z$. The parallel scheme for the Metropolis algorithm relies on the relative positions within the lattice. For example, in a cubic lattice when considering only nearest neighbor interactions, we can divide sites into three classes based on the remainder of their positions $(i+j+k)$ modulo 3, and each class can be run in parallel.

The nudged elastic band (NEB) method is a chain method to compute the minimum energy path (MEP) between two states. Initially, a chain comprising multiple images, each representing a copy of the magnetization, is constructed, and then the whole system is relaxed. The two end images corresponding to the initial and final states are fixed, representing the energy states specified by the user. The system, encompassing all free images, undergoes relaxation to minimize the total energy, akin to relaxing a magnetic system using the LLG equation with the precession term deactivated. A notable distinction lies in the effective field: in the LLG equation, it stems from the functional derivative of the system energy concerning magnetization, whereas in NEB, the effective field of each image additionally incorporates the influence of its adjacent neighbors (i.e., images $n-1$ and $n+1$). The so-called tangents describe this influence: only the perpendicular part of the effective field is retained when relaxing the entire system.[46]

## 8. Verifications and performance

### 8.1. A magnetic moment under an external magnetic field

The LLG equation is nonlinear. The simplest case is the precession motion of a magnetic moment under an external magnetic field. Assuming the external field is along with the $z$-axis and the initial state is $\boldsymbol{m}_0 = (1,0,0)$, then we have

$$\begin{aligned} m_x(t) &= \cos(\tilde{\gamma} H_z t)/\cosh(\alpha\tilde{\gamma} H_z t), \\ m_y(t) &= \sin(\tilde{\gamma} H_z t)/\cosh(\alpha\tilde{\gamma} H_z t), \\ m_z(t) &= \tanh(\alpha\tilde{\gamma} H_z t), \end{aligned} \tag{53}$$

where $\tilde{\gamma} = \gamma/(1+\alpha^2)$. Figure 3 shows the precessional motion of the macrospin under an external magnetic field where the (dashed) lines represent the analytical prediction [Eq. (53)]. The macrospin will align with the external field after dissipating its energy.

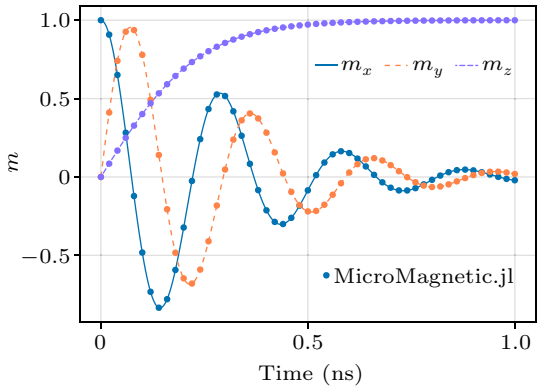



**Fig. 3.** The precession motion of a magnetic moment under an external field with $H_z = 1\times10^5$ A·m$^{-1}$. The parameters used are damping constant $\alpha = 0.5$ and gyromagnetic ratio $\gamma = 2.21\times10^5$ m·A$^{-1}$·s$^{-1}$.

The analytical results provided by Eq. (53) enable us to evaluate the performance of different integration algorithms. We compared the classical Runge–Kutta method with projection and one utilizing a Cayley transformation. The absolute error of the precessional motion at $t = 1$ ns for both approaches is depicted in Fig. 4, with the absolute error defined as $|\boldsymbol{m}_{\text{an}} - \boldsymbol{m}|$. The Cayley transform version performs much better than the projection method for the classical Runge–Kutta scheme.

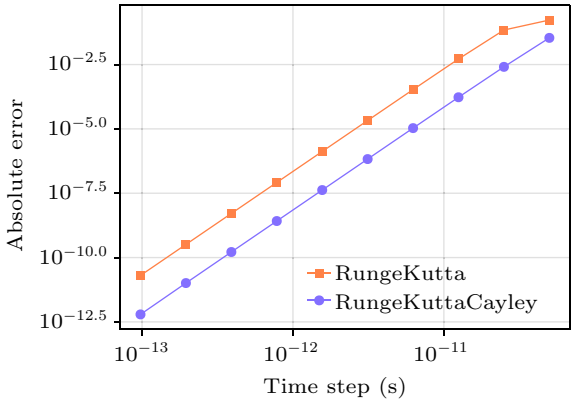



**Fig. 4.** The absolute error of the precession motion of a magnetic moment under an external field at $t = 1$ ns. A small damping $\alpha = 0.05$ is used.

### 8.2. Domain-wall motion under currents

A few exact spatiotemporal solutions for the LLG equation have been reported in the literature. One example is a 1D head-to-head domain wall driven by STT under an arbitrary time dependence function $u = u(t)$[22,47]

$$\dot{\phi} = \frac{(\alpha-\beta)u(t)}{(1+\alpha^2)\Delta}, \quad \dot{z}_* = -\frac{(1+\alpha\beta)u(t)}{(1+\alpha^2)}, \tag{54}$$

where $\dot{z}_*$ is the domain wall center, $\phi$ is the domain wall tilt angle, and $\Delta = \sqrt{A/K}$ is the width of the domain wall.

To validate MicroMagnetic.jl against the analytical solution [Eq. (54)], we apply a time-dependent current represented as $u(t) = u_0 \mathrm{e}^{-bt}\cos(\omega t)$ to the system in our simulation, where $b = 5\times10^8$ s$^{-1}$ and $\omega = 2\times10^9$ s$^{-1}$ are employed. We

conduct simulations with the parameters specific to permalloy: the saturation magnetization $M_s = 8 \times 10^5$ A·m$^{-1}$, the exchange constant $A = 1.3 \times 10^{-11}$ J·m$^{-1}$, and an effective anisotropy $K = 1 \times 10^5$ J·m$^{-3}$. We maintain a fixed damping constant $\alpha = 0.1$ throughout the simulations while varying $\beta$. As depicted in Fig. 5, the comparison between the domain-wall tilt angle $\phi$ obtained using MicroMagnetic.jl and the analytical equation (54) demonstrates a strong agreement.

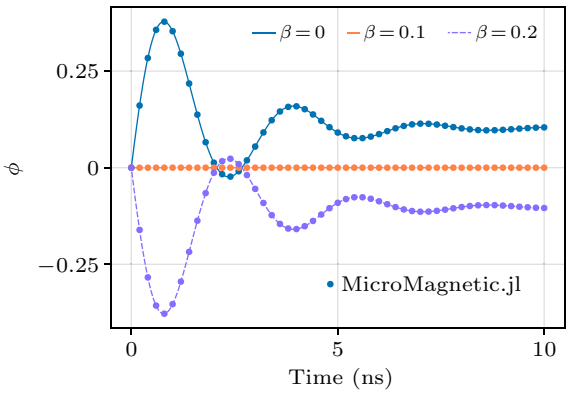



**Fig. 5.** A comparison between the simulation and the analytical solution [Eq. (54)] for the motion of a head-to-head domain wall.

### 8.3. Equilibrium distribution of a nanoparticle

As shown in Ref. [22], we consider a nanoparticle with an effective uniaxial anisotropy along $z$-direction and its energy density reads

$$u = K(1 - m_z^2). \tag{55}$$

In the equilibrium state, the probability distribution function (PDF) $P_{\mathrm{eq}}(m_z)$ satisfies $P_{\mathrm{eq}}(m_z) \propto \exp[-uV/(k_{\mathrm{B}}T)]$. Hence, we have

$$P_{\mathrm{eq}}(m_z) = \frac{1}{Z} \mathrm{e}^{-\chi(1-m_z^2)}, \tag{56}$$

where $\chi = KV/(k_{\mathrm{B}}T)$ and $Z = \int \mathrm{e}^{-\chi(1-m_z^2)} \mathrm{d}m_z$ is the partition function. Assume the volume $V$ of the particle is $V = 2.8 \times 10^{-26}$ nm$^3$, $M_s = 1.42 \times 10^6$ A·m$^{-1}$ and $K = 7.2 \times 10^5$ J·m$^{-3}$. We obtain $Z = 0.428$ for $T = 300$ K. Figure 6 shows the equilibrium probability distribution $P_{\mathrm{eq}}(m_z)$ of a nanoparticle at $T = 300$ K, where $\alpha = 0.1$ is used in the simulation.

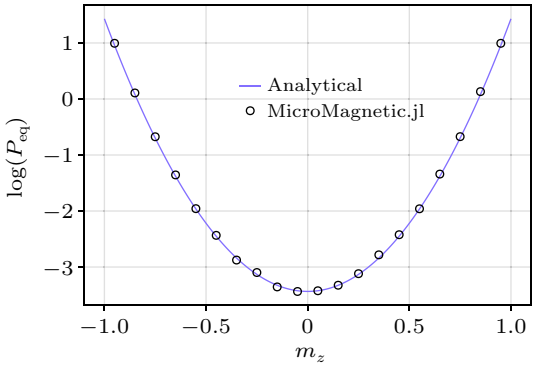



**Fig. 6.** The equilibrium probability distribution $P_{\mathrm{eq}}(m_z)$ of a nanoparticle at $T = 300$ K.

### 8.4. Monte Carlo simulation

Besides directly solving the stochastic LLG equation, in MicroMagnetic.jl, we can also use Monte Carlo to compute the $M$–$T$ curve. For the atomistic model with $z$ nearest neighbors, the relation between exchange constant and $T_c$ reads

$$J = \frac{3k_{\mathrm{B}}T_c}{\varepsilon z}, \tag{57}$$

where $\varepsilon$ is a correction factor and for 3D classical Heisenberg model $\varepsilon \approx 0.719$.[48] Figure 7 presents the calculated average magnetization $m$ and magnetic susceptibility $\chi$ as functions of temperature, using the Monte Carlo method with a cubic mesh of size $N = 30 \times 30 \times 30$. The magnetic susceptibility is computed as

$$\chi = \frac{N}{T}\left[\langle m^2\rangle - \langle m\rangle^2\right]. \tag{58}$$

The critical temperature $T_c \sim 431$ K, determined for $J = 300k_{\mathrm{B}}$ using Eq. (57), is indicated by the dashed vertical line in Fig. 7. It can be observed that the temperature corresponding to the maximum value of $\chi$ closely matches the theoretical prediction.

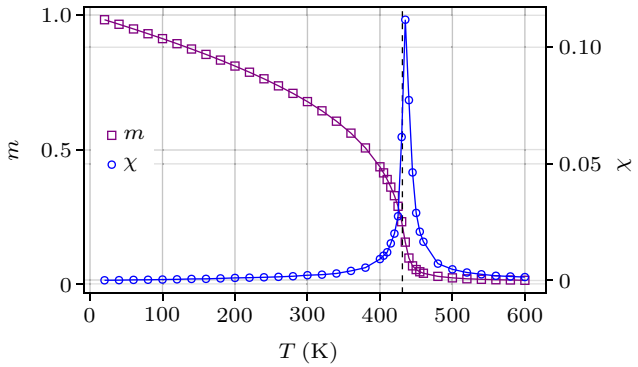



**Fig. 7.** The simulated temperature-dependent magnetization and susceptibility using Monte Carlo methods.

### 8.5. Standard problem 4

Micromagnetic standard problem 4 is a benchmark designed to validate the accuracy of micromagnetic simulations. The system under study is a thin film of permalloy with dimensions of 500 nm in length, 125 nm in width, and 3 nm in thickness. Standard problem 4 consists of two parts. The first part involves relaxing the system from an initial uniform state $\boldsymbol{m}_0 = (1, 0.25, 0.1)$, where the system's energy is iteratively minimized until the change in magnetization falls below a specified threshold, ultimately forming an "S" state. After achieving the "S" state, the next step is to apply an external magnetic field $\boldsymbol{H} = (-24.6\ \mathrm{mT}, 4.3\ \mathrm{mT}, 0)$ and observe the resulting magnetization dynamics. Figure 8 shows the evolution of the average magnetization as a function of time after applying the external magnetic field, using both OOMMF and MicroMagnetic.jl. The results demonstrate a strong agreement between the calculated magnetizations from both methods.

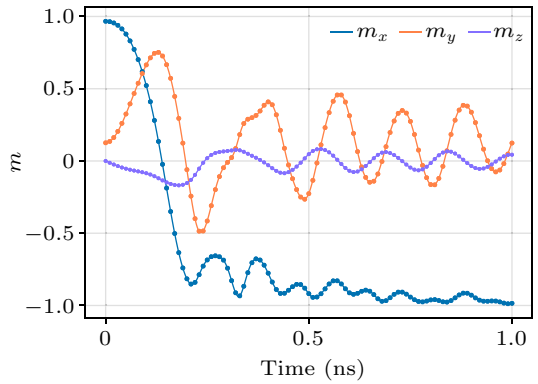



**Fig. 8.** The calculation of the standard problem 4 using OOMMF (lines) and MicroMagnetic.jl (dots).

### 8.6. Performance

In micromagnetic simulations, the most time-consuming component is typically the computation of the demagnetizing field. Despite being accelerated by FFT, this calculation still dominates the total simulation time. To evaluate the performance of MicroMagnetic.jl, we compared it with MuMax3. Figure 9 presents the performance comparison between the two, using an $N \times N \times 1$ system. The results indicate that on the NVIDIA A800 GPU, both MuMax3 and MicroMagnetic.jl achieve throughput rates of up to 1000 million cells per second, with MicroMagnetic.jl performing similarly to MuMax3.

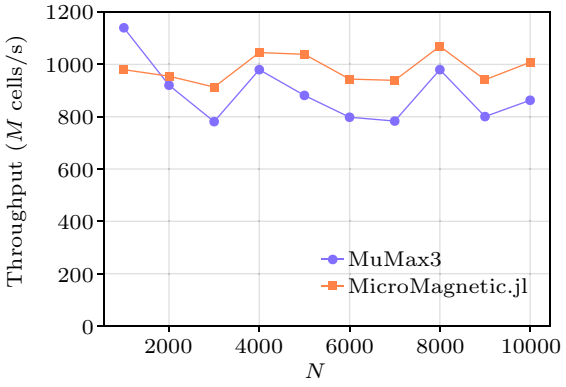



**Fig. 9.** The throughput of MuMax3 and MicroMagnetic.jl on an NVIDIA GPU (A800 SXM4 80 GB). The system size is $N \times N \times 1$, and demagnetization, exchange, and Zeeman interactions are considered. The Henu integrators are used for testing.

## 9. Summary

In conclusion, MicroMagnetic.jl has been introduced as a Julia package designed for micromagnetic and atomistic simulations. With support for CPU and various GPU platforms, researchers can efficiently explore magnetic structures and phenomena at the micrometer scale. MicroMagnetic.jl's open-source nature and ease of extensibility are intended to foster collaboration and innovation, inviting developers to contribute code and expand its functionality. MicroMagnetic.jl's design maximizes user flexibility, making it a versatile toolset for researchers seeking advancements in the study of magnetic materials and devices.

## Program availability

MicroMagnetic.jl is an open-source Julia package licensed under the MIT license, and it can be installed directly through Julia's package manager, `Pkg`. The source code is available on GitHub at https://github.com/MagneticSimulation/MicroMagnetic.jl and in the Science Data Bank at https://doi.org/10.57760/sciencedb.j00113.00138.

## Acknowledgments

Project supported by the National Key R&D Program of China (Grant No. 2022YFA1403603), the Strategic Priority Research Program of Chinese Academy of Sciences (Grant No. XDB33030100), the National Natural Science Fund for Distinguished Young Scholar (Grant No. 52325105), the National Natural Science Foundation of China (Grant Nos. 12374098, 11974021, and 12241406), and the CAS Project for Young Scientists in Basic Research (Grant No. YSBR-084).

## References

[1] Kronmüller H 2007 *Handbook of Magnetism and Advanced Magnetic Materials* (Kronmüller H and Parkin S, Ed.) (Chichester, UK: John Wiley & Sons, Ltd)

[2] Leliaert J and Mulkers J 2019 *J. Appl. Phys.* **125** 180901

[3] Rezende S M 2020 *Fundamentals of Magnonics* (vol. 969) (Cham: Springer International Publishing)

[4] Flebus B, Grundler D, Rana B, Otani Y, Barsukov I, Barman A, Gubbiotti G, Landeros P, Akerman J, Ebels U S, Pirro P, Demidov V E, Schultheiss K, Csaba G, Wang Q, Nikonov D E, Ciubotaru F, Che P, Hertel R, Ono T, Afanasiev D, Mentink J H, Rasing T, Hillebrands B, Viola Kusminskiy S, Zhang W, Du C R, Finco A, Van Der Sar T, Luo Y K, Shiota Y, Sklenar J, Yu T and Rao J 2024 *J. Phys.: Condens. Matter* **36** 363501

[5] Grollier J, Querlioz D, Camsari K Y, Everschor-Sitte K, Fukami S and Stiles M D 2020 *Nat. Electron.* **3** 360

[6] Abert C 2019 *Euro. Phys. J. B* **92** 120

[7] Barla P, Joshi V K and Bhat S 2021 *Journal of Computational Electronics* **20** 805

[8] Miltat J E and Donahue M J 2007 *Handbook of Magnetism and Advanced Magnetic Materials* (Kronmüller H and Parkin S, Ed.) (Chichester, UK: John Wiley & Sons, Ltd)

[9] Schrefl T, Hrkac G and Bance S 2007 *Handbook of Magnetism and Advanced Magnetic Materials* Vol. 2

[10] Donahue M and Porter D 1999 OOMMF User's Guide, Version 1.0

[11] Vansteenkiste A, Leliaert J, Dvornik M, Garcia-Sanchez F and Van Waeyenberge B 2014 *AIP Advances* **4** 107133

[12] Bisotti M A, Cortés-Ortuño D, Pepper R, Wang W, Beg M, Kluyver T and Fangohr H 2018 *J. Open Res. Softw.* **6** 22

[13] Scholz W, Fidler J, Schrefl T, Suess D, Dittrich R, Forster H and Tsiantos V 2003 *Computational Materials Science* **28** 366

[14] Fischbacher T, Franchin M, Bordignon G and Fangohr H 2007 *IEEE Transactions on Magnetics* **43** 2896

[15] Pfeiler C M, Ruggeri M, Stiftner B, Exl L, Hochsteger M, Hrkac G, Schöberl J, Mauser N J and Praetorius D 2020 *Computer Physics Communications* **248** 106965

[16] Bruckner F, Koraltan S, Abert C and Suess D 2023 *Scientific Reports* **13** 12054

[17] Besard T, Churavy V, Edelman A and Sutter B D 2019 *Advances in Engineering Software* **132** 29

[18] Churavy V, Aluthge D, Smirnov A, Schloss J, Samaroo J, Wilcox L C, Byrne S, Besard T, Ramadhan A, Waruszewski M, Schaub S D, Meredith, Moses W, Bolewski J, Constantinou N C, Ng M, Bauer C, Schanen M, johnbcoughlin, Shah V B, Dixit V K, Chor T, Holy T, Arakaki T, Yalburgi S, Liu R and Haraldsson P 2024 JuliaGPU/KernelAbstractions.jl: V0.9.18 [object Object]

[19] Bisotti M A, Beg M, Wang W, Albert M, Chernyshenko D, Cortés-Ortuño D, Pepper R A, Vousden M, Carey R, Fuchs H, Johansen A, Balaban G, Breth L, Kluyver T and Fangohr H 2018 FinMag: Finite-element micromagnetic simulation tool Zenodo

[20] Newell A J, Williams W and Dunlop D J 1993 *Journal of Geophysical Research* **98** 9551

[21] Abert C, Bruckner F, Vogler C, Windl R, Thanhoffer R and Suess D 2015 *J. Magn. Magn. Mater.* **387** 13

[22] Wang W 2015 *Computer Simulation Studies of Complex Magnetic Materials* (Ph.D. thesis) (University of Southampton)

[23] Abert C, Selke G, Kruger B and Drews A 2012 *IEEE Transactions on Magnetics* **48** 1105

[24] Mühlbauer S, Binz B, Jonietz F, Pfleiderer C, Rosch A, Neubauer A, Georgii R and Böni P 2009 *Science* **323** 915

[25] Huang S X and Chien C L 2012 *Phys. Rev. Lett.* **108** 267201

[26] Cortés-Ortuño D, Beg M, Nehruji V, Breth L, Pepper R, Kluyver T, Downing G, Hesjedal T, Hatton P, Lancaster T, Hertel R, Hovorka O and Fangohr H 2018 *New J. Phys.* **20** 113015

[27] Vedmedenko E Y, Riego P, Arregi J A and Berger A 2019 *Phys. Rev. Lett.* **122** 257202

[28] Han D S, Lee K, Hanke J P, Mokrousov Y, Kim K W, Yoo W, Van Hees Y L W, Kim T W, Lavrijsen R, You C Y, Swagten H J M, Jung M H and Kläui M 2019 *Nat. Mater.* **18** 703

[29] Tatara G, Kohno H and Shibata J 2008 *Physics Reports* **468** 213

[30] Nowak U 2007 *Handbook of Magnetism and Advanced Magnetic Materials* 1st Edn. (Kronmüller H and Parkin S, Ed.) (Wiley)

[31] Skubic B, Hellsvik J, Nordström L and Eriksson O 2008 *J. Phys.: Condens. Matter* **20** 315203

[32] Evans R F L, Fan W J, Chureemart P, Ostler T, Ellis M O and Chantrell R W 2014 *J. Phys.: Condens. Matter* **26** 103202

[33] Dzyaloshinskii I 1958 *J. Phys. Chem. Solids* **4** 241

[34] Moriya T 1960 *Phys. Rev.* **120** 91

[35] Rohart S and Thiaville A 2013 *Phys. Rev. B* **88** 184422

[36] Gilbert T L 2004 *IEEE Transactions on Magnetics* **40** 3443

[37] Press W H and Teukolsky S A 1992 *Computers in Physics* **6** 188

[38] Slonczewski J 1996 *J. Magn. Magn. Mater.* **159** L1

[39] Zhang S and Li Z 2004 *Phys. Rev. Lett.* **93** 127204

[40] Meo A, Cronshaw C E, Jenkins S, Lees A and Evans R F L 2023 *J. Phys.: Condens. Matter* **35** 025801

[41] Krishnaprasad P S and Tan X 2001 *Physica B* **306** 195

[42] Iserles A and Zanna A 2000 *LMS Journal of Computation and Mathematics* **3** 44

[43] Diele F, Lopez L and Peluso R 1998 *Advances in Computational Mathematics* **8** 317

[44] Abert C, Wautischer G, Bruckner F, Satz A and Suess D 2014 *J. Appl. Phys.* **116** 123908

[45] Exl L, Bance S, Reichel F, Schrefl T, Peter Stimming H and Mauser N J 2014 *J. Appl. Phys.* **115** 128

[46] Cortes D I 2017 *Computational Simulations of Complex Chiral Magnetic Structures* (Ph.D. thesis) (University of Southampton)

[47] Wang W, Zhang Z, APepper R, Mu C, Zhou Y and Fangohr H 2018 *J. Phys.: Condens. Matter* **30** 015801

[48] Garanin D A 1996 *Phys. Rev. B* **53** 11593